

Universality of biochemical feedback and its application to immune cells

Amir Erez,^{1,*} Tommy A. Byrd,^{2,*} Robert M. Vogel,³ Curtis Peterson,⁴
Michael Vennettilli,² Grégoire Altan-Bonnet,¹ and Andrew Mugler^{2,†}

¹*Immunodynamics Group, Cancer and Inflammation Program, National Cancer Institute,
National Institutes of Health, Bethesda, Maryland 20814, USA*

²*Department of Physics and Astronomy, Purdue University, West Lafayette, Indiana 47907, USA*

³*IBM T. J. Watson Research Center, Yorktown Heights, New York 10598, USA*

⁴*Department of Physics and School of Mathematical and Statistical Sciences,
Arizona State University, Tempe, Arizona 85287*

Positive feedback in biochemical networks can lead to a bifurcation in state space. Universality implies that if molecules are well mixed, this bifurcation should exhibit the critical scaling behavior of the Ising universality class in the mean-field limit. Making this statement quantitative requires the appropriate mapping between the biochemical parameters and the Ising parameters. Here we derive this mapping rigorously and uniquely for a broad class of stochastic birth-death models with feedback, and show that the expected static and dynamic critical exponents emerge. The generality of the mapping allows us to extract the order parameter, effective temperature, magnetic field, and heat capacity from T cell flow cytometry data without needing to know the underlying molecular details. We find that T cells obey critical scaling relations and exhibit critical slowing down, and that the heat capacity determines molecule number from fluorescence data. We demonstrate that critical scaling holds even as our system is driven out of its steady state, via the Kibble-Zurek mechanism for driven critical systems. Our approach places a ubiquitous biological mechanism into a known class of physical systems and is immediately applicable to other biological data.

Positive feedback is ubiquitous in biochemical networks and can lead to a bifurcation from a monostable to a bistable cellular state [1–4]. The bifurcation point is similar to an Ising-type critical point in physical systems such as fluids, magnets, and superconductors, where a disordered state transitions to one of two ordered states at a critical temperature [5]. In fact, universality tells us that the two should not just be similar, they should be the same: because they are both bifurcating systems, both types of systems should exhibit the same critical scaling exponents and therefore belong to the same universality class [5]. Although this powerful idea has allowed diverse physical phenomena to be united into specific behavioral classes, the application of universality to biological systems is still developing [6–11].

Biological tools such as flow cytometry, fluorescence microscopy, and DNA sequencing allow reliable experimental estimates of probability distributions, inspiring researchers to seek to apply insights from statistical physics to biological data. In particular, recent studies have demonstrated that biological systems on many scales, from molecules [12], to cells [13–16], to populations [17, 18], exhibit signatures consistent with physical systems near a critical point. However, many of these studies do not focus on identification of critical exponents or universality class, and some of these signatures, particularly scaling laws, can arise even far from a critical point [19, 20] or can be alternatively explained without relying on criticality [21]. Part of the problem is that

the identification of appropriate scaling variables from data can be ambiguous, and one is often left looking for scaling relationships in an unguided way. To rigorously test for universality in biological systems, a theoretical framework is needed that can identify scaling variables from first principles and generate falsifiable predictions for experiments.

Here we provide a general framework for investigating the critical behavior of biochemical feedback and apply it to both published and new data on T cells. We consider a generic stochastic model in which feedback is encapsulated in a birth-death process. Because our model treats molecules as well mixed, we expect the critical exponents of the Ising universality class in its mean-field limit. We derive the mapping between the biochemical and Ising parameters, and demonstrate that these exponents indeed emerge. Our theory allows us to extract effective thermodynamic quantities from experimental data without needing to fit to any mechanistic model of the system. Applied to T cells, this process reveals fundamental new insights, including an interpretation of drug-induced changes in terms of an effective temperature and field, a novel way to estimate molecule number from fluorescence intensity, and evidence of critical scaling and critical slowing down. Our results give a unifying picture of critical behavior in cells with feedback and lay the groundwork for extensions to other biological phenomena.

I. RESULTS

We consider a reaction network in a cell where X is the molecular species of interest, and the other species

*These authors contributed equally.

†Electronic address: amugler@purdue.edu

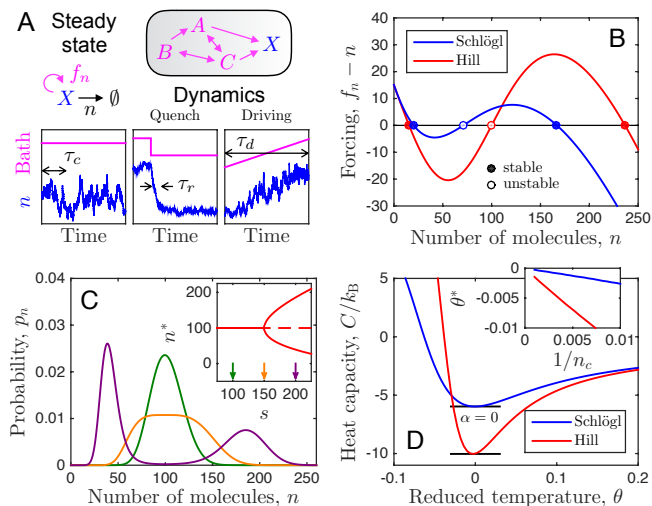
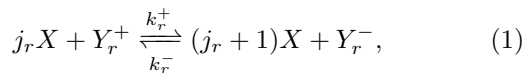


FIG. 1: Model behavior. (A) We consider a model of biochemical feedback in either a static or a dynamic intracellular environment. (B) Feedback produces either one or two stable steady states. (C) The molecule number distribution is peaked around these states or flat at the critical point. (D) We find that the heat capacity (Eq. 6) is minimized at the critical point. Parameters: $H = 3$ in B, C, D; $K = 126$ and $a = 100 - s/3$ in B, C; $s = 255$ in B; $n_c = 500$ and $h = 0$ in D (see Table I).

A, B, C , etc. form a chemical bath for X (Fig. 1A, top right). The reactions of interest produce or degrade an X molecule, can involve the bath species, and in principle are reversible. We allow for nonlinear feedback on X , meaning that the production of an X molecule in a particular reaction might require a certain number of X molecules as reactants. This leads to a general set of R reactions of the form



where in each reaction $r \in \{1, 2, \dots, R\}$, the $j_r \in \{0, 1, 2, \dots\}$ are stoichiometric integers describing the nonlinearity, k_r^\pm are the forward (+) and backward (-) reaction rates, and Y_r^\pm represent bath species involved as reactants (+) or products (-). A simple and well-studied special case of Eq. 1 is Schlögl's second model¹ [6, 7, 23–28], in which X is either produced spontaneously from bath species A , or in a trimolecular reaction from two existing X molecules and bath species B (i.e., $R = 2$, $j_1 = 0$, $j_2 = 2$, $Y_1^+ = A$, $Y_2^+ = B$, and $Y_1^- = Y_2^- = \emptyset$). We assume that molecules are well-mixed and that reaction rates and numbers of bath molecules are constant.

Eq. 1 describes a single-species birth-death process

with feedback. A deterministic description will admit either one or two stable steady states (Fig. 1B), and a corresponding stochastic description will produce a steady-state distribution that is peaked around the deterministic value(s) (Fig. 1C). Stochasticity is intrinsic to the reactions and therefore scales with the reaction propensities, a feature that can be captured by [29–32]: a Langevin description with multiplicative noise terms; a Fokker-Planck description with propensity-dependent diffusion and drift; or a master equation, which we use here. The fact that fluctuations scale with propensities makes biochemical noise distinct from thermal noise, in which fluctuations are set by a constant temperature bath [29, 31]. Yet, universality raises the expectation that this distinction should not matter near the critical point. Indeed, we show in the Supplementary Information (SI) and Fig. 5 that the stochastic description given below is equivalent to a Ginzburg-Landau description [33, 34] if and only if the system is near its critical point. At the critical point the system is out of equilibrium because in equilibrium, detailed balance reduces the steady state of Eq. 1 to the Poisson distribution, corresponding to no feedback [28, 30].

The master equation for the probability of observing n molecules of species X is

$$\dot{p}_n = b_{n-1}p_{n-1} + d_{n+1}p_{n+1} - (b_n + d_n)p_n, \quad (2)$$

where $b_n = \sum_{r=1}^R J_{rn}^+$ and $d_n = \sum_{r=1}^R J_{rn}^-$ are the total birth and death propensities, and $J_{rn}^+ = k_r^+ n_r^+ n! / (n - j_r)!$ and $J_{rn}^- = k_r^- n_r^- n! / (n - j_r - 1)!$ are the forward and backward propensities of each reaction pair. Here n_r^\pm are the numbers of molecules of the bath species involved in reaction r , and the factorials account for the number of ways that X molecules can meet in a reaction. The steady state of Eq. 2 is [29, 30]

$$p_n = p_0 \prod_{j=1}^n \frac{b_{j-1}}{d_j} = \frac{p_0}{n!} \prod_{j=1}^n f_j, \quad (3)$$

where $p_0^{-1} = \sum_{n=0}^{\infty} (1/n!) \prod_{j=1}^n f_j$ is set by normalization. In the second step of Eq. 3 we recognize that p_n depends only on the ratio of birth and death propensities, and therefore we define an effective birth propensity $f_n \equiv n b_{n-1} / d_n$ corresponding to spontaneous death with propensity n (Fig. 1A, top left). The function f_n encodes the feedback. Importantly, Eq. 3 allows calculation of f_n from data, as detailed later on.

In general, f_n is an arbitrary, nonlinear function governed by the reaction network. For Schlögl's second model, the feedback function is $f_n = [aK^2 + s(n-1)(n-2)] / [(n-1)(n-2) + K^2]$, where we have introduced the dimensionless quantities $a \equiv k_1^+ n_A / k_1^-$, $s \equiv k_2^+ n_B / k_2^-$, and $K^2 \equiv k_1^- / k_2^-$. As a ubiquitous example we also consider the Hill function $f_n = a + s n^H / (n^H + K^H)$ with coefficient H . The quantity $f_n - n$ determines the dynamic stability: depending on the parameters, there can be either one or two stable states n^* where $f_n - n$ vanishes

¹ Not to be confused Schlögl's first model in the same paper [6], which is known to be in the directed percolation universality class [7, 22].

with negative slope (Fig. 1B). Along particular parameter directions a transition from a monostable to a bistable regime occurs at a bifurcation point (Fig. 1C inset). As anticipated, these regimes correspond to unimodal and bimodal distributions p_n , respectively, while the bifurcation point corresponds to a distribution that is flat on top (Fig. 1C).

A. Ising mapping and critical exponents

We expect the critical exponents β , γ , and δ to emerge from the deterministic stability condition $f_{n^*} - n^* = 0$, or equivalently the maxima of the distribution p_n [31]. We expand f_n to third order around a point n_c that we are free to choose. Taking n_c such that $f'_{n_c} = 0$ as in the Ginzburg–Landau critical point, the condition becomes $f_{n_c} + f'_{n_c}(n^* - n_c) + f''_{n_c}(n^* - n_c)^2/2! + f'''_{n_c}(n^* - n_c)^3/3! - n^* = 0$. We then define the parameters

$$m \equiv \frac{n^* - n_c}{n_c}, \quad h \equiv \frac{2(f_{n_c} - n_c)}{-f'''_{n_c} n_c^3}, \quad \theta \equiv \frac{2(1 - f'_{n_c})}{-f'''_{n_c} n_c^2}, \quad (4)$$

in terms of which the condition becomes

$$h - \theta m - m^3/3 = 0. \quad (5)$$

Eq. 5 is equivalent to the expansion of the Ising mean field equation $m = \tanh[(m + h)/(1 + \theta)]$ for small magnetization m , where $\theta = (T - T_c)/T_c$ is the reduced temperature, and h is the dimensionless magnetic field [34]. Therefore in our system we interpret m as the order parameter, θ as an effective reduced temperature, and h as an effective field. Positive (negative) θ drives the system to the unimodal (bimodal) state, while positive (negative) h biases the system to high (low) molecule numbers. For example, Fig. 1C is constructed by varying θ with $h = 0$ (see Table I). Despite the fact that $h = 0$, an asymmetry persists in p_n because fluctuations scale with molecule number, as is particularly evident from the bimodal case in Fig. 1C. Eq. 5 demonstrates that our system has the same scaling exponents $\beta = 1/2$, $\gamma = 1$, and $\delta = 3$ as the Ising universality class in the mean-field limit [34], confirmed using the maxima of p_n for the Schlögl and Hill models in Fig. 6.

The exponent α differs fundamentally from β , γ , and δ because it depends on the entire distribution p_n , not just the maxima. Specifically, α concerns the heat capacity, $C|_{h=0} \sim |\theta|^{-\alpha}$, which depends on the entropy S and thus p_n . The equilibrium definition $C = T\partial_T S$ generalizes to a nonequilibrium system like ours when one uses the Shannon entropy $S = -k_B \sum_n p_n \log p_n$ [35]. Since $T = (1 + \theta)T_c$, we have $C = (1 + \theta)\partial_\theta S$, or

$$\frac{C}{k_B} = -(1 + \theta) \sum_{n=0}^{\infty} p_n (1 + \log p_n) \left(\psi_n - \sum_{j=0}^{\infty} p_j \psi_j \right), \quad (6)$$

where $\psi_n \equiv (1/2)f'''_{n_c} n_c^2 \sum_{j=1}^n (j - n_c)/f_j$. Eq. 6 follows from performing the θ derivative using the expression

in Eq. 3, the expansion above Eq. 4, and the definition of θ (Eq. 4). We see in Fig. 1D that when $h = 0$, C exhibits a minimum at θ^* , and the inset shows that θ^* vanishes as the system size increases, $n_c \rightarrow \infty$. This implies that $C|_{h=0} \sim |\theta|^0$ to sub-quadratic order in θ , or $\alpha = 0$, again consistent with the Ising universality class in its mean-field limit. Interestingly, whereas C is discontinuous in the mean-field Ising model [34] and constant in the van der Waals model of a fluid [5], it is minimized here; nevertheless, in all cases $\alpha = 0$. Fig. 1D shows that C is negative near $\theta = 0$; negative heat capacity is a well-known feature of nonequilibrium steady states [36–38].

B. Critical scaling in immune cells

A key advantage of our theory is that calculating the Ising parameters requires only knowledge of the distribution and not any details of the underlying model apart from its birth-death nature. To see this, we rewrite Eq. 3 as

$$f_n = n p_n / p_{n-1}, \quad (7)$$

which gives the feedback function f_n directly from the distribution p_n [39]. Once f_n is obtained, the Ising parameters follow via Eqs. 4 and 6. This allows us to investigate scaling properties directly from experimental data, without needing to know the underlying details of the molecular network.

Therefore, we test our theory using previously published data from T cells of doubly phosphorylated ERK (ppERK) [4]. As previously shown [4], chemotherapy drugs alter feedback in the MAP-kinase signaling cascade by inhibiting key enzymes (MEK and SRC). In particular, low (high) doses produce bimodal (unimodal) distributions of ppERK abundance, measured as fluorescence intensity I by flow cytometry (Fig. 2A). We extract the Ising parameters from these data using the following procedure (see SI and Fig. 7 for full details). First, we set $n = I/I_1$ to convert $p(I)$ to p_n , where the intensity of one molecule I_1 is determined as described later in this section. Next, because the experimental distributions are long-tailed, we convert Eqs. 4 and 7 to $\log I$ space for numerical stability (Fig. 2A inset). Finally, we smooth the distribution using a Savitzky–Golay filter [40] with window size W . This procedure requires the adjustable parameter W/L , where L is the number of $\log I$ bins, and we show that results are robust to W/L (SI and Fig. 8). Several findings validate the analysis. First, distributions with $\theta > 0$ are unimodal (high dose), while bimodal distributions (low dose) have $\theta < 0$ (Fig. 2A). Second, as expected from Fig. 1B, we see in Fig. 2B that the quantity $f(I) - I$ has one stable state when the distribution is unimodal (light cyan), and two stable states when the distribution is bimodal (dark cyan). Third, consistent with previous results from fitting p_n with a Gaussian mixture model [4], but here without fitting to

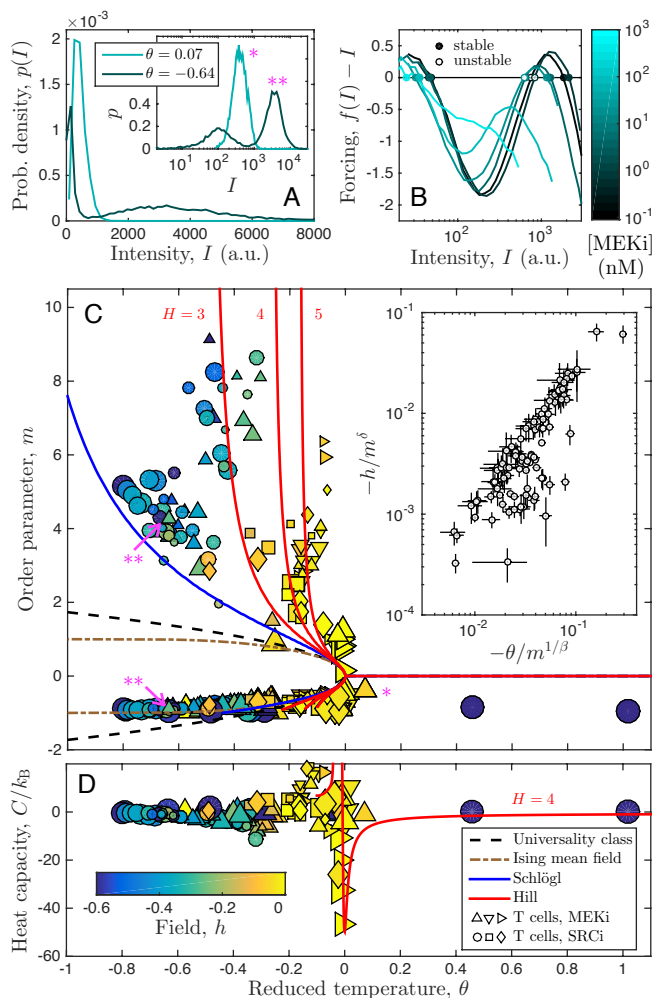


FIG. 2: Experimental analysis and critical scaling. (A) Experimental distributions of T cell ppERK fluorescence intensity [4] are bimodal (unimodal) under low (high) doses of inhibitor. Legend: θ calculated by Eq. 4. (B) Experimental feedback functions give Ising parameters (Eqs. 4 and 6). (C, D) Order parameter and heat capacity data agree with theory, particularly for $h \approx 0$ (yellow data) where theory is shown. See Table II for drugs (shape) and doses (size). C inset: $m > 0$ data with standard error from $25 \leq W \leq 35$ and $L = 100$ as in Fig. 3. Magenta asterisks indicate points in C corresponding to distributions in A. Theory uses $f_{n^*} - n^* = 0$ in C and ensures $a > 0$ and $s > 0$ in C (for $m < 0$) and D, bounding θ from below (Table I). Parameters: $W = 25$ and $L = 100$ in B, C, D; $I_1 = 0.1$ in D; $h = 0$ and $n_c = 7,300$ (mean experimental value) for Schlögl and Hill models.

a model, we find that the location of the high stable state changes with MEK inhibitor but not SRC inhibitor (Fig. 9).

Fig. 2C shows the $h = 0$ predictions from the theory (blue and red), the mean-field Ising model (brown), and the universality class to which they belong (Eq. 5; black). All coincide at the critical point ($m = \theta = 0$) and have the same scaling nearby [$m \sim (-\theta)^\beta$ for small $-\theta$]. However, far from the critical point there are notable

differences, as here the behavior is no longer constrained by the universality class. Specifically, whereas the lower branches ($m < 0$) of the biochemical and Ising models both obey $m \geq -1$ because the number of molecules and up-spins is nonnegative, respectively (Eq. 4); the upper branch ($m > 0$) of the Ising model obeys $m \leq 1$, while those of the biochemical models rise steeply. The reason is that whereas the total number of spins is fixed, the number of molecules is unbounded from above in a birth-death process. The data points in Fig. 2C show m and θ from the experimental data for all drugs (shape) and doses (size), colored according to h . Most data have $\theta \lesssim 0$ because doses are sufficiently low to maintain a non-negligible high state, and $h \lesssim 0$ because the long tail is indistinguishable from a low-molecule-number bias in the peak. We see that the data agree with the predictions in several important ways: (i) no data exist between the branches; (ii) data near $m = \theta = 0$ have $h \approx 0$ (yellow); (iii) the data closely follow the lower branch and obey $m \geq -1$; and (iv) the data exhibit the steep rise of the upper branches in the biochemical models, particularly the Hill function with $H \sim 4$.

Empirical estimation of the critical exponents requires careful tuning of the system to the critical point, a difficult task even in nonliving systems [41], and these data were not acquired with such tuning in mind. However, a scaling prediction exists for Ising universality class that does not require such tuning: a plot of the rescaled variables h/m^δ vs. $\theta/m^{1/\beta}$ should collapse to a single function [42]. The inset of Fig. 2C shows these variables from the data in the upper branch of Fig. 2C.² We see that with limited exceptions the data do indeed collapse to a single function over more than a decade in $\theta/m^{1/\beta}$ and more than two decades in h/m^δ , as predicted.

Fig. 2D shows the $h = 0$ prediction for the heat capacity C with $H = 4$ (red). A key feature of the prediction is the presence of a global minimum at $\theta = 0$. We see that this feature is indeed exhibited by the data, particularly for $h \approx 0$ (yellow data) as expected. We find that the data exhibit the minimum irrespective of the choice of I_1 over four orders of magnitude (Fig. 10). Importantly, however, the depth of the minimum agrees with that of the theory only for $I_1 \sim 0.1$ as in Fig. 2D. This value of I_1 corresponds to $n^* \approx 35,000$ molecules in the high state without inhibition (see SI), in agreement with previous measurements on these cells [43, 44]. This suggests that the heat capacity provides a novel way to estimate absolute molecule number from fluorescence data.

² The lower branch is sensitive to cells' autofluorescence at low intensities (a well-known phenomenon in flow cytometry), which may affect the scaling.

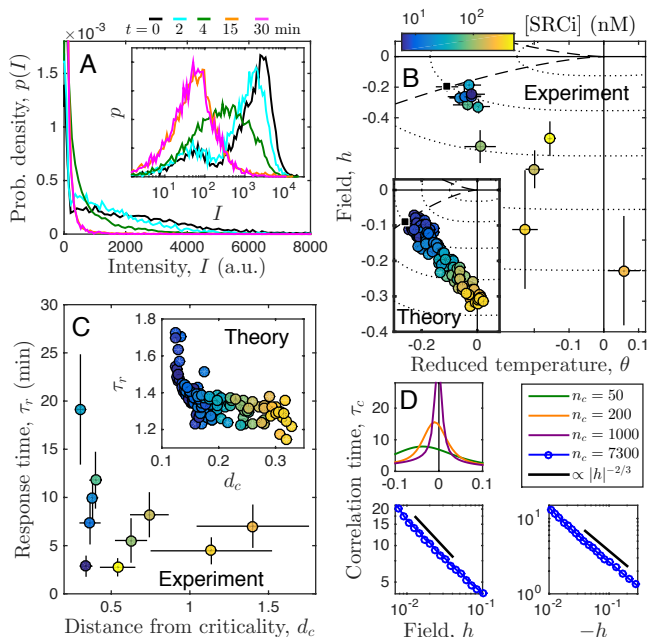


FIG. 3: Experimental dynamics and critical slowing down. (A) Experimental distributions of T cell ppERK fluorescence intensity measured at times after addition of SRC inhibitor. Here $[\text{SRCi}] = 333$ nM (see Fig. 11 for all doses). (B) Ising θ and h extracted from initial (black square) and final distributions (colored circles) for $[\text{SRCi}]$ doses (color bar). Error bars: standard error from results with $25 \leq W \leq 35$ and $L = 100$ because beyond this range low-dose points deviate from initial point indicating over- or under-filtering. Black dashed line: separates bimodal (left) from unimodal (right) regime according to Eq. 5. Black dotted lines: contours of equal distance from criticality, defined $d_c = [(\theta^{\beta\delta})^2 + h^2]^{1/2}$ because τ_c scales identically with $\theta^{\beta\delta}$ as with h (Eq. 8). Inset: same for Schlogl model with $n_c = 7,300$, colored according to distance from initial point. (C) Experimental response time τ_r decreases with distance from criticality d_c . Error bars: propagated from B (d_c) or standard deviation of Riemann sums spanning left- to right-endpoint methods (τ_r). Inset: same for Schlogl model. (D) Schlogl model exhibits critical slowing down with expected mean-field exponents $\nu z / \beta\delta = 2/3$. Here $\theta = 0$. Top left: eigenfunctions; cutoff $N = \max(100, 3n_c)$. Bottom: batch means; 250 (left) or 1,000 (right) trajectories; duration $T = 10^5$; batch time $\tau_b = 2,176$. For all Schlogl model results, time is in units of $1/k_1^-$.

C. Immune cell dynamics and critical slowing down

Cell environments are generally dynamic, with changes that can occur suddenly or gradually in time (Fig. 1A, bottom right). We expect that if a change takes a cell near its critical point, the cell's response should suffer from critical slowing down [33, 45]. To test this expectation, we use flow cytometry to measure the ppERK distribution at various times after the addition of a SRC inhibitor (see SI for experimental methods). This protocol corresponds to a sudden change, or quench, from no drug to a specific dose of drug. When the dose is small,

the distribution hardly changes (Fig. 11); whereas when the dose is large, the distribution changes significantly over a finite response time (Fig. 3A).

Because the cells usually complete their response within about 10 minutes [4], we treat both the initial and the final ($t_{\max} = 30$ min) distributions as steady states, allowing us to use the theory to extract their θ and h values. We see in Fig. 3B that the effect of the drug is to take cells from an initial state with $\theta < 0$ and $h \approx 0$ (black square) corresponding to a bimodal distribution, to a final state with $\theta \approx 0$ and $h < 0$ (yellow circles) corresponding to a unimodal distribution with a long tail. Different drug doses correspond to different final states, each at different distances d_c from the critical point $\theta = h = 0$, as illustrated by the dotted lines in Fig. 3B. If critical slowing down occurs, we expect that doses with larger d_c will have smaller response times. We define the response time as the relaxation timescale of the mean intensity, $\tau_r = \Delta \bar{I}(0)^{-1} \int_0^{t_{\max}} dt \Delta \bar{I}(t)$, where $\Delta \bar{I}(t) = \bar{I}(t) - \bar{I}(t_{\max})$. We see in Fig. 3C that as d_c increases, τ_r decreases, as expected.

To confirm that the observations in Fig. 3C are indicative of critical slowing down, we return to the birth-death model. Critical slowing down is defined by a divergence of the correlation time τ_c (Fig. 1A, bottom left) at the critical point according to [46]

$$\tau_c|_{h=0} \sim |\theta|^{-\nu z}, \quad \tau_c|_{\theta=0} \sim |h|^{-\nu z / \beta\delta}, \quad (8)$$

where we expect $\nu z = 1$ for the mean-field universality class [33, 34].³ We calculate $\tau_c = \kappa(0)^{-1} \int_0^\infty dt \kappa(t)$, with correlation function $\kappa(\Delta t) = \langle n(t)n(t+\Delta t) \rangle - \bar{n}^2$, for Schlogl's second model in steady state either numerically using the eigenfunctions of Eq. 2, or by simulation using the Gillespie algorithm [47] and the method of batch means [48] (see SI and Fig. 12). Determining νz requires only one of the relations in Eq. 8, and we choose the latter because the former encounters an ambiguity between inter- and intra-peak correlations for bimodal distributions ($\theta < 0$) at finite system size. We see in Fig. 3D that τ_c diverges with h in the model at a location and with a scaling that approach the expected values of $h = 0$ and $\nu z / \beta\delta = 2/3$, respectively, for large n_c . We then apply a quench to the simulation from an initial θ and h location to one of many final locations, indicated by the black square and colored circles, respectively, in the inset of Fig. 3B. We measure the response time $\tau_r = \Delta \bar{n}(0)^{-1} \int_0^{t_{\max}} dt \Delta \bar{n}(t)$, where $\Delta \bar{n}(t) = \bar{n}(t) - \bar{n}(t_{\max})$ and $t_{\max} \gg \tau_r$. We see in the inset of Fig. 3C that τ_r decreases with d_c as in the experiments. This demonstrates that critical slowing down extends the response time in the model, in a similar way to the quench experiments.

³ Because our model is well-mixed, the correlation length exponent ν is not meaningful on its own, but only in combination with the dynamic exponent z .

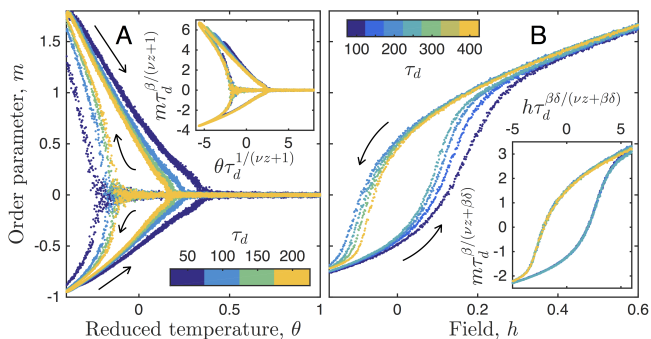


FIG. 4: Dynamic driving and Kibble-Zurek collapse. (A) Ising θ or (B) h in Schlögl model increases or decreases (arrows) linearly over time τ_d (colors). Order parameter m lags behind due to critical slowing down, resulting in hysteresis, e.g. supercooling (A left curves) or superheating (A right curves). Insets: Rescaled curves collapse as predicted. In A, $h = 0$; in B, $\theta = 0$. Each point is computed via Eq. 4 from mode n^* (or $n_1^* < n_c$ and $n_2^* > n_c$ in A) of 10^5 simulation trajectories. Finite-size correction (SI): $n_c = 10\tau_d$ in A, $n_c = 22\tau_d^{4/5}$ in B. Time is in units of $1/k_1^-$.

D. Dynamic driving and the Kibble-Zurek mechanism

While some environmental changes are sudden, others are gradual (Fig. 1A, bottom right). If a gradual change drives a system through its critical point, critical slowing down will delay the system's response such that no matter how gradual the change, there will come a point when the response will lag behind the driving. The Kibble-Zurek mechanism describes these lagging dynamics in terms of the critical exponents [49, 50]. Although in a biological setting the driving protocol could take many forms, terms beyond the leading-order linear term do not change the critical dynamics [51]. Therefore we investigate linear driving across the critical point, $\theta(t) = \theta_0 - (\theta_f - \theta_0)t/\tau_d$ or $h(t) = h_0 - (h_f - h_0)t/\tau_d$, where τ_d is the driving time.

The idea of the Kibble-Zurek mechanism is that far from the critical point, the change in the system's correlation time due to the driving, over a correlation time, is small compared to the correlation time itself, $(d\tau_c/dt)\tau_c \ll \tau_c$, and therefore the system responds adiabatically. However, as the system is driven closer to the critical point, these two quantities are on the same order, or $d\tau_c/dt \sim 1$, and the system begins to lag. Applying this condition to Eq. 8 with $\theta(t)$ or $h(t)$ as above, we obtain $\theta \sim \tau_d^{-1/(\nu z+1)}$ or $h \sim \tau_d^{-\beta\delta/(\nu z+\beta\delta)}$. Since $m \sim (-\theta)^\beta$ or $m \sim h^{1/\delta}$ near criticality, we have $m \sim \tau_d^{-\beta/(\nu z+1)}$ or $m \sim \tau_d^{-\beta/(\nu z+\beta\delta)}$. Therefore, even if the system is driven at different timescales τ_d , the Kibble-Zurek mechanism predicts that plots of $m\tau_d^{\beta/(\nu z+1)}$ vs. $\theta\tau_d^{1/(\nu z+1)}$ or $m\tau_d^{\beta/(\nu z+\beta\delta)}$ vs. $h\tau_d^{\beta\delta/(\nu z+\beta\delta)}$ should collapse onto universal curves.

We test this prediction using the Gillespie simulation

of Schlögl's second model. We drive either θ or h in either an increasing or decreasing direction for various τ_d , and we correct for finite-size effects using the fact that $\tau_c \sim n_c^{1/2}$ for large n_c (see SI and Fig. 13). The results are shown in Fig. 4. We see that in both cases, the order parameter lags in different directions and by different amounts, depending on the driving direction and timescale, respectively (Fig. 4A and B). Yet we see that the rescaled variables indeed collapse onto single, direction-dependent curves within a large region near criticality, as predicted (Fig. 4A and B insets). We also see that the collapse begins to fail far from criticality, especially on the upper branch ($m > 0$) where deviations from the universality class are larger, as expected. This demonstrates that our nonequilibrium birth-death model exhibits the Kibble-Zurek collapse of critical physical systems. Together with our previous findings, this result suggests that such a collapse should emerge in biological experiments where environmental parameters (e.g., drug dose) are dynamically controlled.

II. DISCUSSION

For a broad class of biochemical systems with feedback, we have made rigorous the notion of universality, namely that the bifurcation point exhibits the critical scaling properties of the Ising universality class in the mean-field limit. The upshot of our approach is that it provides the order parameter, temperature, external field, and heat capacity from experimental distributions without needing to know the molecular details. By applying the approach to T cell flow cytometry data, we have discovered that the heat capacity encodes the information about molecule number, and that cells exhibit critical scaling and critical slowing down in their response to drugs. The universal nature of biochemical feedback extends to systems driven out of their nonequilibrium steady state, as demonstrated by the Kibble-Zurek mechanism.

How does the heat capacity extract the conversion between fluorescence intensity and molecule number? α is the only static exponent that is a function of p_n instead of just its maxima, and therefore the plot of C vs. θ (Fig. 2D) contains information about noise. Imagine if the distribution were Poissonian: then the relation $\sigma_I^2/\bar{I}^2 = \sigma_n^2/\bar{n}^2 = 1/\bar{n} = I_1/\bar{I}$ would provide the conversion factor I_1 given knowledge of the mean \bar{I} and the noise σ_I^2 . Here, the heat capacity is extracting similar information, but for a critical system.

Our analysis of the heat capacity confirms that the number of ppERK molecules per cell is in the tens of thousands. Large molecule number reduces intrinsic noise as $\sigma_n/\bar{n} \sim 1/\sqrt{\bar{n}}$, as mentioned above. On the other hand, our analysis of critical slowing down reveals that the correlation time near criticality grows with molecule number as $\tau_c \sim \sqrt{n_c}$. This suggests that cells may face a tradeoff in terms of precision vs. response time when

responding to changes near criticality [52].

The theory assumes only birth-death reactions and neglects more complex mechanisms such as bursting [53, 54], extrinsic noise [31], or cell-to-cell variability [55]. These mechanisms are known to produce long tails and may be responsible for the long tails observed in the experimental data (Figs. 2A and 3A). Nonetheless, we find that the birth-death model captures the essential features of the data, both near criticality (Fig. 2D) and far from it (Figs. 2C and 3), and that the long tails manifest as negative values of the effective magnetic field.

Our work provides tools that can be used for a broader exploration of critical behavior in biological systems. Our approach is applicable to any experimental dataset that exhibits unimodal and bimodal abundance distributions, and could lead to a unified picture of diverse cell types and environmental perturbations in terms of an effective temperature and field. Natural extensions include generalizing the theory to systems that are not well-mixed, such as intracellular compartments or communicating populations, to investigate space-dependent universal behavior and its biological implications.

III. METHODS

See SI for descriptions of the experimental data analysis, experimental procedures, calculation of the correlation time, and finite-size correction during dynamic driving. Data, code, and MIFlowCyt record are at <https://github.com/AmirErez/UniversalityImmunePNAS>.

IV. ACKNOWLEDGMENTS

We thank Anushya Chandran for helpful communications. This work was supported by Human Frontier Science Program grant LT000123/2014 (Amir Erez), Simons Foundation grant 376198 (T.A.B. and A.M.), NSF REU grant PHY-1460899 (C.P.) and by the Intramural Research Program of the NIH, Center for Cancer Research, NCI.

-
- [1] Mitrophanov AY, Groisman EA (2008) Positive feedback in cellular control systems. *Bioessays* 30(6):542–555.
- [2] Tkačik G, Walczak AM, Bialek W (2012) Optimizing information flow in small genetic networks. iii. a self-interacting gene. *Physical Review E* 85(4):041903.
- [3] Das J, et al. (2009) Digital signaling and hysteresis characterize ras activation in lymphoid cells. *Cell* 136(2):337–351.
- [4] Vogel RM, Erez A, Altan-Bonnet G (2016) Dichotomy of cellular inhibition by small-molecule inhibitors revealed by single-cell analysis. *Nature Communications* 7:12428.
- [5] Goldenfeld N (1992) *Lectures on phase transitions and the renormalization group*. (Addison-Wesley, Advanced Book Program, Reading).
- [6] Schlögl F (1972) Chemical reaction models for non-equilibrium phase transitions. *Zeitschrift für Physik* 253(2):147–161.
- [7] Grassberger P (1982) On phase transitions in Schlögl’s second model. *Zeitschrift für Physik B Condensed Matter* 47(4):365–374.
- [8] Ohtsuki T, Keyes T (1987) Nonequilibrium critical phenomena in one-component reaction-diffusion systems. *Physical Review A* 35(6):2697.
- [9] Pal M, Ghosh S, Bose I (2014) Non-genetic heterogeneity, criticality and cell differentiation. *Physical biology* 12(1):016001.
- [10] Ridden SJ, Chang HH, Zygalkakis KC, MacArthur BD (2015) Entropy, ergodicity, and stem cell multipotency. *Physical review letters* 115(20):208103.
- [11] Qian H, Ao P, Tu Y, Wang J (2016) A framework towards understanding mesoscopic phenomena: Emergent unpredictability, symmetry breaking and dynamics across scales. *Chemical Physics Letters* 665:153–161.
- [12] Mora T, Walczak AM, Bialek W, Callan CG (2010) Maximum entropy models for antibody diversity. *Proceedings of the National Academy of Sciences* 107(12):5405–5410.
- [13] Kastner DB, Baccus SA, Sharpee TO (2015) Critical and maximally informative encoding between neural populations in the retina. *Proceedings of the National Academy of Sciences* 112(8):2533–2538.
- [14] Krotov D, Dubuis JO, Gregor T, Bialek W (2014) Morphogenesis at criticality. *Proceedings of the National Academy of Sciences* 111(10):3683–3688.
- [15] De Palo G, Yi D, Endres R (2016) A critical-like collective state leads to long-range cell communication in *Drosophila* aggregation. *bioRxiv* p. 086538.
- [16] Chen X, Dong X, Be’er A, Swinney HL, Zhang H (2012) Scale-invariant correlations in dynamic bacterial clusters. *Physical Review Letters* 108(14):148101.
- [17] Bialek W, et al. (2014) Social interactions dominate speed control in poising natural flocks near criticality. *Proceedings of the National Academy of Sciences* 111(20):7212–7217.
- [18] Attanasi A, et al. (2014) Finite-size scaling as a way to probe near-criticality in natural swarms. *Physical Review Letters* 113(23):238102.
- [19] Belitz D, Kirkpatrick T, Vojta T (2005) How generic scale invariance influences quantum and classical phase transitions. *Reviews of modern physics* 77(2):579.
- [20] Kessler DA, Levine H (2015) Generic criticality in ecological and neuronal networks. *arXiv preprint arXiv:1508.02414*.
- [21] Schwab DJ, Nemenman I, Mehta P (2014) Zipf’s law and criticality in multivariate data without fine-tuning. *Physical Review Letters* 113(6):068102.
- [22] Cardy JL, Sugar R (1980) Directed percolation and reggeon field theory. *Journal of Physics A: Mathematical and General* 13(12):L423.
- [23] Dewel G, Walgraef D, Borckmans P (1977) Renormalization group approach to chemical instabilities. *Zeitschrift*

- für Physik B Condensed Matter 28(3):235–237.
- [24] Nicolis G, Malek-Mansour M (1980) Systematic analysis of the multivariate master equation for a reaction-diffusion system. *Journal of Statistical Physics* 22(4):495–512.
- [25] Brachet M, Tirapegui E (1981) On the critical behaviour of the Schlögl model. *Physics Letters A* 81(4):211–214.
- [26] Prakash S, Nicolis G (1997) Dynamics of the Schlögl models on lattices of low spatial dimension. *Journal of Statistical Physics* 86(5):1289–1311.
- [27] Liu DJ, Guo X, Evans JW (2007) Quadratic contact process: Phase separation with interface-orientation-dependent equistability. *Physical Review Letters* 98(5):050601.
- [28] Vellela M, Qian H (2009) Stochastic dynamics and non-equilibrium thermodynamics of a bistable chemical system: the schlögl model revisited. *Journal of the Royal Society Interface* 6(39):925–940.
- [29] Van Kampen NG (1992) *Stochastic processes in physics and chemistry*. (Elsevier).
- [30] Gardiner CW (1985) *Handbook of stochastic methods*. (Springer Berlin).
- [31] Horsthemke W, Lefever R (1984) *Noise-induced transitions*. (Springer).
- [32] Gillespie DT (2000) The chemical langevin equation. *The Journal of Chemical Physics* 113(1):297–306.
- [33] Hohenberg PC, Halperin BI (1977) Theory of dynamic critical phenomena. *Reviews of Modern Physics* 49(3):435.
- [34] Kopietz P, Bartosch L, Schütz F (2010) *Introduction to the functional renormalization group*. (Springer) Vol. 798.
- [35] Mandal D (2013) Nonequilibrium heat capacity. *Physical Review E* 88(6):062135.
- [36] Zia R, Praestgaard E, Mouritsen O (2002) Getting more from pushing less: Negative specific heat and conductivity in nonequilibrium steady states. *American Journal of Physics* 70(4):384–392.
- [37] Boksenbojm E, Maes C, Netočný K, Pešek J (2011) Heat capacity in nonequilibrium steady states. *EPL (Europhysics Letters)* 96(4):40001.
- [38] Bisquert J (2005) Master equation approach to the nonequilibrium negative specific heat at the glass transition. *American Journal of Physics* 73(8):735–741.
- [39] Walczak AM, Mugler A, Wiggins CH (2009) A stochastic spectral analysis of transcriptional regulatory cascades. *Proceedings of the National Academy of Sciences* 106(16):6529–6534.
- [40] Savitzky A, Golay MJ (1964) Smoothing and differentiation of data by simplified least squares procedures. *Analytical Chemistry* 36(8):1627–1639.
- [41] Heller P (1967) Experimental investigations of critical phenomena. *Reports on Progress in Physics* 30(2):731.
- [42] Gaunt D, Domb C (1970) Equation of state of the ising model near the critical point. *Journal of Physics C: Solid State Physics* 3(7):1442.
- [43] Altan-Bonnet G, Germain RN (2005) Modeling t cell antigen discrimination based on feedback control of digital erk responses. *PLoS Biology* 3(11):e356.
- [44] Hukelmann JL, et al. (2015) The cytotoxic t cell proteome and its shaping by the kinase mtor. *Nature immunology*.
- [45] Dai L, Vorselen D, Korolev KS, Gore J (2012) Generic indicators for loss of resilience before a tipping point leading to population collapse. *Science* 336(6085):1175–1177.
- [46] Pathria RK, Beale PD (2011) *Statistical mechanics*. (Academic Press).
- [47] Gillespie DT (1977) Exact stochastic simulation of coupled chemical reactions. *The journal of physical chemistry* 81(25):2340–2361.
- [48] Thompson MB (2010) A comparison of methods for computing autocorrelation time. *arXiv preprint arXiv:1011.0175*.
- [49] Kibble TW (1976) Topology of cosmic domains and strings. *J. Phys. A* 9(8):1387.
- [50] Zurek WH (1985) Cosmological experiments in superfluid helium? *Nature* 317(6037):505–508.
- [51] Chandran A, Erez A, Gubser SS, Sondhi S (2012) Kibble-zurek problem: Universality and the scaling limit. *Physical Review B* 86(6):064304.
- [52] Skoge M, Meir Y, Wingreen NS (2011) Dynamics of cooperativity in chemical sensing among cell-surface receptors. *Physical review letters* 107(17):178101.
- [53] Friedman N, Cai L, Xie XS (2006) Linking stochastic dynamics to population distribution: an analytical framework of gene expression. *Physical Review Letters* 97(16):168302.
- [54] Mugler A, Walczak AM, Wiggins CH (2009) Spectral solutions to stochastic models of gene expression with bursts and regulation. *Physical Review E* 80(4):041921.
- [55] Cotari JW, Voisinne G, Dar OE, Karabacak V, Altan-Bonnet G (2013) Cell-to-cell variability analysis dissects the plasticity of signaling of common γ chain cytokines in t cells. *Science Signaling* 6(266):ra17–ra17.

Supplementary information

Ginzburg-Landau near criticality

Ginzburg-Landau theory suggests that we write Eq. 3 of the main text as $p_n \propto e^{-U_n}$, where U_n is a dimensionless energy, and

$$F_n = -\partial_n U_n = \partial_n \log p_n \quad (9)$$

is the associated dimensionless force. At the same time, Fig. 2B of the main text independently suggests a force that is proportional to $f_n - n$, namely

$$\tilde{F}_n = -\partial_n \tilde{U}_n = \frac{f_n - n}{n_c} \quad (10)$$

where the proportionality factor $1/n_c$ is set as described below. In general, F_n and \tilde{F}_n are different. Indeed, van Kampen (Ref. [29] of the main text) emphasizes that only for thermal or diffusion-like processes, where the scale of fluctuations is set by a constant temperature, are U_n and \tilde{U}_n (and thus F_n and \tilde{F}_n) the same; for birth-death processes like the one we study here, where fluctuations scale with molecule number, they are different. However, we see in Fig. 5A that at the critical point (orange), the difference $\Delta F_n = F_n - \tilde{F}_n$ becomes small, especially around n_c . We quantify this observation by computing the squared curvature $(\Delta F''_{n_c})^2$, and indeed, in Fig. 5B we see that this measure vanishes at the critical point.

This behavior can be understood from Eq. 3 of the main text. For large n we have

$$F_n = \partial_n \log p_n \approx \log f_n - \log n = \log \left[1 + \frac{f_n - n}{n} \right]. \quad (11)$$

At the critical point, f_n is tangent to n at n_c . This creates the largest range of n over which $f_n - n$ is small, which permits the expansion of F_n around n_c as $F_n \approx (f_n - n)/n_c = \tilde{F}_n$ (also setting the proportionality factor). Thus, at the critical point the two forces agree, and the stochastic model behaves like an Ginzburg-Landau system.

Experimental data analysis

Due to the long-tailed nature of the experimental molecule number distributions, it is more numerically stable to analyze them in log space. Here we provide the necessary conversions between functions of the molecule number from the theory, and functions of the log intensity from the experiments. In this section, prime denotes a derivative of a function with respect to its argument (n for f ; ℓ for q , Q , and ϕ).

The intensity is proportional to molecule number, $I = I_1 n$, where I_1 is the intensity of one molecule. We record

and analyze the log intensity $\ell = \log I$. Therefore we have

$$\ell = \log(I_1 n), \quad n = \frac{e^\ell}{I_1}. \quad (12)$$

The molecule number distribution is p_n . Denote the distribution of ℓ as $q(\ell)$. Approximating n as continuous, probability conservation requires $p_n dn = q(\ell) d\ell$. Therefore

$$q(\ell) = \frac{p_n}{d\ell/dn} = np_n. \quad (13)$$

The feedback function is related to the probability distribution according to $f_n = np_n/p_{n-1}$ (Eq. 7 of the main text). Using Eq. 13, the feedback function is written

$$f_n = \frac{np_n}{p_{n-1}} = (n-1) \frac{np_n}{(n-1)p_{n-1}} = (n-1) \frac{q(\ell)}{q(\tilde{\ell})}, \quad (14)$$

where, using Eq. 12,

$$\tilde{\ell} = \log[I_1(n-1)] = \log(I_1 n) + \log(1-\epsilon) \approx \ell - \epsilon. \quad (15)$$

The last steps define $\epsilon \equiv 1/n$ and assume that for most values of n with appreciable probability we have $\epsilon \ll 1$. Therefore Eq. 14 becomes

$$\begin{aligned} f_n &= n(1-\epsilon) \frac{q(\ell)}{q(\ell-\epsilon)} \approx n(1-\epsilon) \frac{q(\ell)}{q(\ell) - \epsilon q'(\ell)} = \frac{n(1-\epsilon)}{1 - \epsilon q'/q} \\ &\approx n(1-\epsilon) \left(1 + \epsilon \frac{q'}{q} \right) \approx n \left[1 + \epsilon \left(\frac{q'}{q} - 1 \right) \right] \\ &= n + \frac{q'}{q} - 1, \end{aligned} \quad (16)$$

where we have kept only to first order in ϵ . Defining $\phi(\ell) \equiv f_n - n$, from Eq. 16 we have

$$\phi(\ell) = f_n - n = \frac{q'}{q} - 1 = Q'. \quad (17)$$

In the last step we define

$$Q(\ell) \equiv -\ell + \log q \quad (18)$$

so that ϕ is computed as a total derivative, which we find more numerically stable.

Maxima are defined by $p'_{n^*} = 0$. Eq. 12 implies

$$\partial_n = I_1 e^{-\ell} \partial_\ell \quad (19)$$

Therefore, using Eqs. 12 and 13, the maxima condition reads

$$\begin{aligned} 0 &= \partial_n p = (I_1 e^{-\ell} \partial_\ell) \left(\frac{q}{n} \right) = I_1 e^{-\ell} \partial_\ell (I_1 e^{-\ell} q) \\ &= I_1^2 e^{-\ell} (-e^{-\ell} q + e^{-\ell} q') = (I_1 e^{-\ell})^2 (q' - q). \end{aligned} \quad (20)$$

We define points ℓ^* by

$$q'(\ell^*) = q(\ell^*). \quad (21)$$

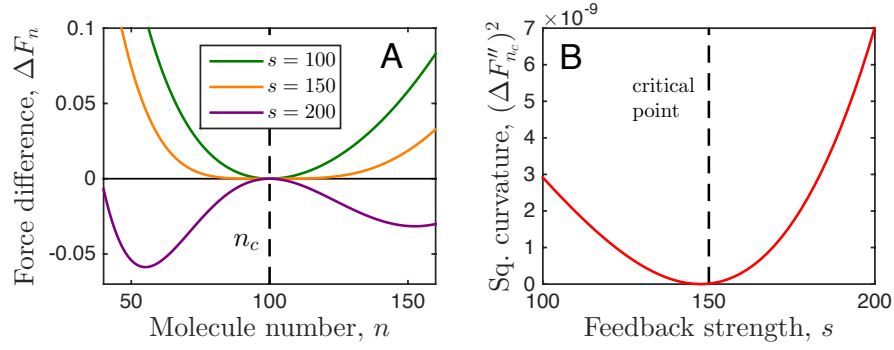


FIG. 5: The stochastic model becomes equivalent to a Ginzburg-Landau description near the critical point. (A) At the critical value of feedback strength s (orange), the difference $\Delta F_n = F_n - \tilde{F}_n$ between the Ginzburg-Landau and the stochastic force becomes small, especially around n_c . (B) Consequently, the squared curvature $(\Delta F''_{n_c})^2$ vanishes at the critical point. Parameters are as in Fig. 2C of the main text: $H = 3$, $K = 126$ and $a = 100 - s/3$.

	Schlögl	Hill
Feedback function	$f_n = \frac{aK^2 + s(n-1)(n-2)}{(n-1)(n-2) + K^2}$	$f_n = a + s \frac{n^H}{n^H + K^H}$
Critical value (at which $f''_{n_c} = 0$)	$n_c = \frac{3}{2} + \frac{1}{6} \sqrt{3(4K^2 - 1)}$	$n_c = K \left(\frac{H-1}{H+1} \right)^{1/H}$
Expansion coefficients	$f_{n_c} = \frac{(3a+s)K^2 - s}{4K^2 - 1}$ $f'_{n_c} = (s-a)K^2 \left(\frac{3}{4K^2 - 1} \right)^{3/2}$ $f'''_{n_c} = -6(s-a)K^2 \left(\frac{3}{4K^2 - 1} \right)^{5/2}$	$f_{n_c} = a + \left(\frac{H-1}{2H} \right) s$ $f'_{n_c} = \frac{(H^2 - 1)s}{4Hn_c}$ $f'''_{n_c} = -\frac{(H^2 - 1)^2 s}{8Hn_c^3}$
Inversion (where $x \equiv 2n_c - 3$)	$K^2 = \frac{1}{4}(3x^2 + 1)$ $s = \frac{3n_c^3(\theta+h) + n_c x^2 + x^3}{3n_c^2 \theta + x^2}$ $a = \frac{(3x^2 + 1)[3n_c^3(\theta+h) + n_c x^2 + x^3] - 4x^5}{(3x^2 + 1)(3n_c^2 \theta + x^2)}$	$K = n_c \left(\frac{H+1}{H-1} \right)^{1/H}$ $s = n_c \frac{16H}{(H^2 - 1)[(H^2 - 1)\theta + 4]}$ $a = n_c \frac{(H-1)[(H+1)^2(\theta+h) + 4]}{(H+1)[(H^2 - 1)\theta + 4]}$

TABLE I: Here we provide the values of n_c and the expansion coefficients f_{n_c} , f'_{n_c} , and f'''_{n_c} , on which θ and h depend via Eq. 4 of the main text, in terms of the biochemical parameters of the Schlögl and Hill models. We also provide the algebraic inverse: expressions for the biochemical parameters a , s , and K in terms of the criticality parameters. In the Hill model H is an additional free parameter.

Equivalently, by Eq. 17, the ℓ^* satisfy

$$\phi(\ell^*) = 0, \quad (22)$$

forcing. The maxima are obtained via Eq. 12:

$$n^* = \frac{e^{\ell^*}}{I_1}. \quad (23)$$

which is consistent with the interpretation of ϕ as the

The critical point n_c is defined by $f''_{n_c} = 0$. Using Eq.

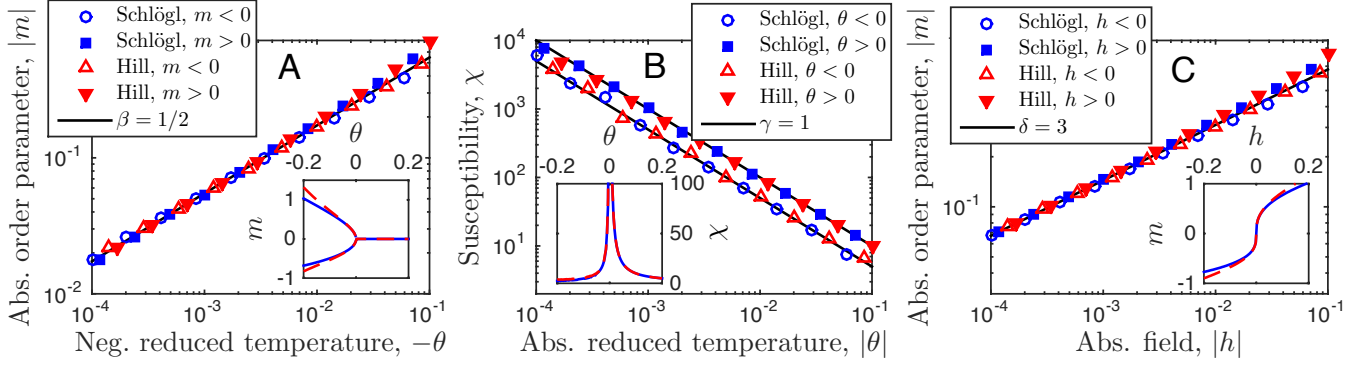


FIG. 6: Critical exponents β , γ , and δ of biochemical feedback model agree with those of Ising universality class in the mean-field limit. Specifically, when $h = 0$, Eq. 5 of the main text becomes $0 = m(\theta + m^2/3)$; thus $m = \pm(-3\theta)^\beta$ when $\theta > 0$ or $\theta < 0$, respectively, with $\beta = 1/2$. Defining the dimensionless susceptibility $\chi \equiv (\partial_h m)_{h=0}$ and differentiating Eq. 5 gives $\chi = \theta^{-\gamma}$ or $\chi = (-2\theta)^{-\gamma}$ for $\theta > 0$ or $\theta < 0$, respectively, with $\gamma = 1$. Finally, when $\theta = 0$, Eq. 5 becomes $m = (3h)^{1/\delta}$, with $\delta = 3$. Panels A, B, and C confirm these scalings, respectively, using the maxima of p_n for the Schlögl and Hill models. Parameters are $H = 3$, $n_c = 500$, $h = 0$ in A and B, and $\theta = 0$ in C. K , a , and s are calculated from n_c , θ , and h according to Eq. 4 of the main text (see Table I). B uses $m < 0$ maximum for $\theta < 0$; results are similar for $m > 0$.

Drug	Inhibits	Dose range (nM)	Shape of point
PD325901	MEK	0.09–1000	Up triangle
AZD6244	MEK	2.4–5000	Down triangle
Trametinib	MEK	0.5–1000	Right triangle
Dasatinib	SRC	0.09–1000	Circle
Bosutinib	SRC	0.5–1000	Square
PP2	SRC	24–50,000	Diamond

TABLE II: Drugs and dose ranges used Figs. 2, 8, and 10. Doses are spaced logarithmically.

19, this condition reads

$$\begin{aligned}
 0 &= \partial_n^2 f = \partial_n^2(\phi + n) = \partial_n^2 \phi = (I_1 e^{-\ell} \partial_\ell)^2 \phi \\
 &= I_1 e^{-\ell} \partial_\ell (I_1 e^{-\ell} \partial_\ell \phi) = I_1^2 e^{-2\ell} (-e^{-\ell} \phi' + e^{-\ell} \phi'') \\
 &= (I_1^2 e^{-2\ell}) (\phi'' - \phi').
 \end{aligned} \tag{24}$$

We define a point ℓ_c by

$$\phi''(\ell_c) = \phi'(\ell_c), \tag{25}$$

and the critical point n_c is obtained via Eq. 12:

$$n_c = \frac{e^{\ell_c}}{I_1}. \tag{26}$$

Numerically we enforce Eq. 25 by writing it as $0 = \partial_\ell(\phi' - \phi)$, and therefore

$$\ell_c = \operatorname{argmax}_\ell (\phi' - \phi). \tag{27}$$

Derivatives of f with respect to n at n_c are related in a straightforward way to derivatives of ϕ with respect to ℓ at ℓ_c . First, the zeroth derivative is, by Eq. 17,

$$f_{n_c} = \phi(\ell_c) + n_c, \tag{28}$$

where n_c is given by Eq. 26. Then, using Eq. 19, the first derivative is

$$\begin{aligned}
 f'_{n_c} &= \partial_n[\phi + n]_{n_c} = \partial_n[\phi]_{n_c} + 1 = [(I_1 e^{-\ell} \partial_\ell)\phi]_{\ell_c} + 1 \\
 &= I_1 e^{-\ell_c} \phi'(\ell_c) + 1 = \frac{\phi'(\ell_c)}{n_c} + 1.
 \end{aligned} \tag{29}$$

Finally, by a similar procedure, the third derivative is

$$\begin{aligned}
 f'''_{n_c} &= \frac{1}{n_c^3} [\phi'''(\ell_c) - 3\phi''(\ell_c) + 2\phi'(\ell_c)] \\
 &= \frac{1}{n_c^3} [\phi'''(\ell_c) - \phi'(\ell_c)],
 \end{aligned} \tag{30}$$

where the second step uses Eq. 25.

Using Eqs. 26, 28-30, and 23, the Ising parameters defined in Eq. 4 of the main text are

$$m = \frac{n^* - n_c}{n_c} = e^{\ell^* - \ell_c} - 1, \tag{31}$$

$$\theta = \frac{2(1 - f'_{n_c})}{-f'''_{n_c} n_c^2} = \frac{-2\phi'(\ell_c)}{\phi'(\ell_c) - \phi'''(\ell_c)}, \tag{32}$$

$$h = \frac{2(f_{n_c} - n_c)}{-f'''_{n_c} n_c^3} = \frac{2\phi(\ell_c)}{\phi'(\ell_c) - \phi'''(\ell_c)}. \tag{33}$$

Note that they do not depend on I_1 .

To estimate derivatives, we apply Savitsky-Golay filtering to $q(\ell)$. Savitsky-Golay filtering replaces each data point with the value of a polynomial of order J that is fit to the data within a window W of the point. Since we require three derivatives of $\phi(\ell)$ (Eqs. 32 and 33), which depends on the first derivative of $q(\ell)$ (Eq. 17), we use the minimum value $J = 4$.

The analysis is demonstrated for an example experimental condition in Fig. 7. In summary, we:

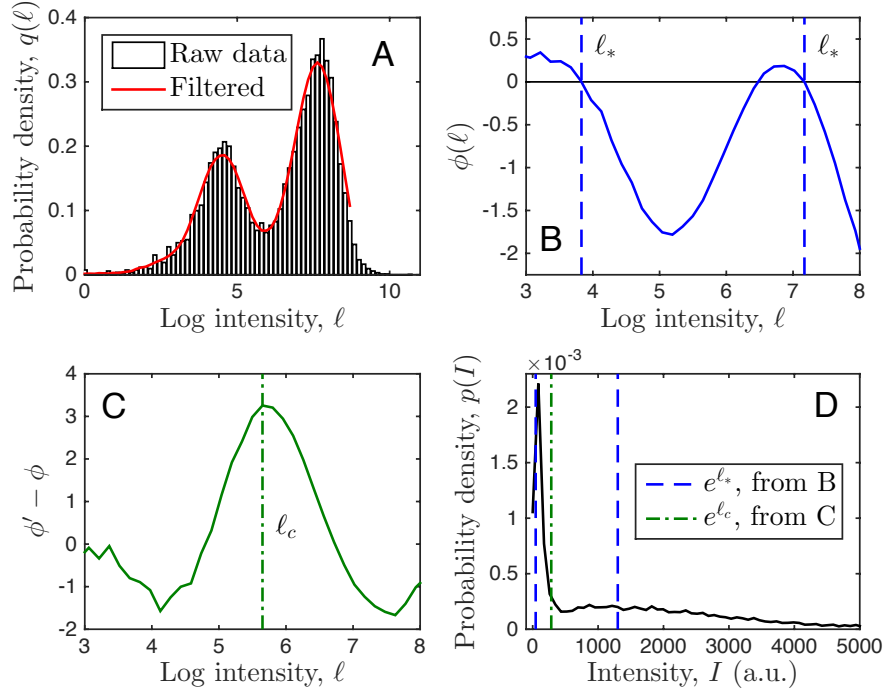


FIG. 7: Demonstration of analysis procedure for 3.4 nM of MEK inhibitor PD325901. (A) Distribution $q(\ell)$ of log intensity ℓ is plotted using $L = 100$ bins and Savitsky-Golay filtered using window of $W = 25$ data points. (B, C) From filtered data, we compute $\phi(\ell)$ to find ℓ^* , and $\phi' - \phi$ to find ℓ_c , as described in the text. (D) ℓ^* and ℓ_c give maxima and critical point of the intensity distribution.

1. plot $q(\ell)$ from the data using L bins (Fig. 7A, black);
2. filter $q(\ell)$ using window W (Fig. 7A, red);
3. compute ℓ^* using Eq. 22 (Fig. 7B);
4. compute ℓ_c using Eq. 27 (Fig. 7C);
5. compute m , θ , and h from ℓ_c , ℓ^* , and ϕ and its derivatives using Eqs. 31-33;
6. compute p_n from the data using I_1 ; and
7. compute C/k_B from p_n , θ , n_c (Eq. 26), f_{n_c}''' (Eq. 30), and f_n (Eq. 16) using Eq. 6 of the main text.

Fig. 7D shows the values of ℓ^* and ℓ_c overtop the intensity distribution $p(I)$. We see that the maxima fall where expected, and the critical point falls between the maxima as expected.

Robustness of results

Typically when working with distributions, the number of bins is an adjustable parameter. However, since here we also filter the distribution, changing the filter window is similar to changing the number of bins. That is, choosing a large number of bins L , but also a large

window size $W < L$, is similar to choosing a small L . Therefore, we choose L to be sufficiently large to resolve the main features of the distribution, then focus on the adjustable parameter W/L . We find that $L = 100$ suffices (although we check L as low as 50 in what follows).

In principle, the parameter W/L varies from 0 to 1. $W/L = 0$ corresponds to no filtering, whereas $W/L = 1$ corresponds to using every data point in the filter, i.e., extreme over-filtering. In the main text we use $W/L = 25/100 = 0.25$ (Fig. 2). Here we investigate the robustness of the results to the value of W/L , focusing in particular on the behavior of the order parameter in Fig. 2C of the main text. As shown in Fig. 8, we vary W/L over the range 0.15 to 0.5 in two ways: we either vary W (Fig. 8A and B) or L (Fig. 8C and D). We see that in both cases, the theory and the experimental data continue to agree in the same ways noted in the main text: (i) no data exist between the branches; (ii) data near $m = \theta = 0$ have $h \approx 0$ (yellow); (iii) the data closely follow the lower branch and obey $m \geq -1$; and (iv) the data exhibit the steep rise of the upper branches in the biochemical models.

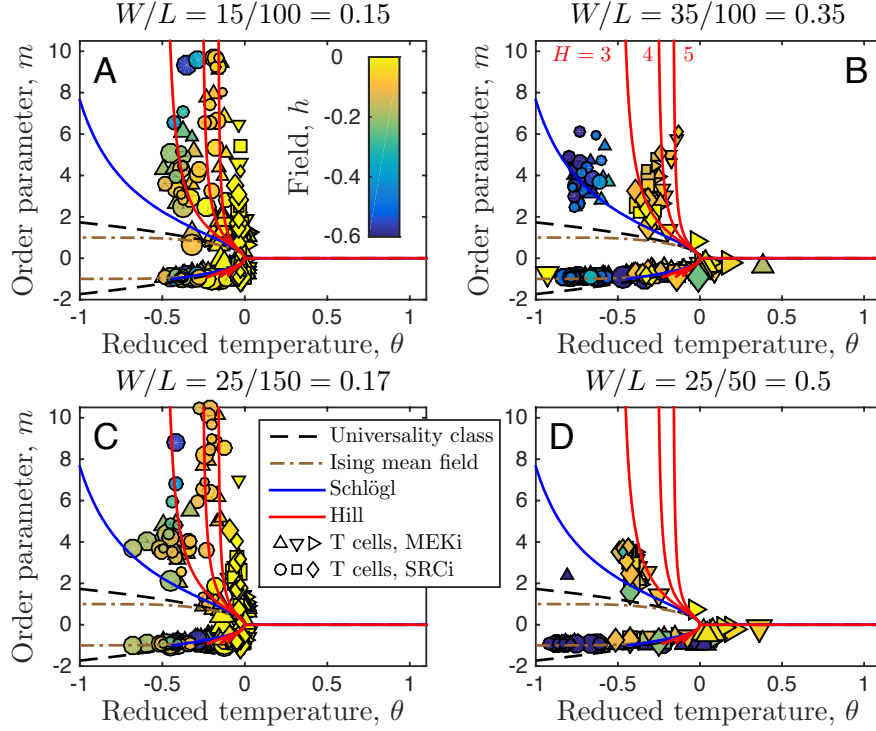


FIG. 8: Main features are robust to choice of W/L , as described in the text. Title of each panel indicates choices of W and L . See Table II for drugs (shape) and doses (size). All theory curves take $h = 0$.

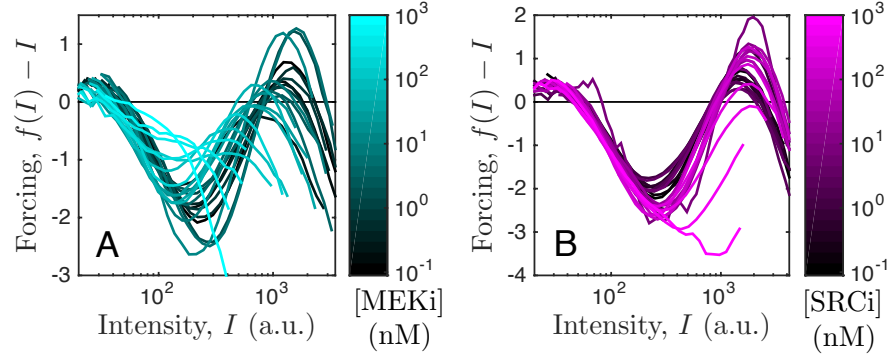


FIG. 9: Forcing function [equivalent to $\phi(\ell)$] at various doses of (A) MEK inhibitor PD325901 and (B) SRC inhibitor Dasatinib. We see that MEK inhibition drives the high-intensity stable fixed point to lower molecule numbers, whereas SRC inhibition does not, as expected from previous work (Ref. [4] of the main text).

Absolute molecule number

Absolute molecule number is set by the conversion factor I_1 . Fig. 10 shows C for the theory and the experimental data using four values of I_1 over four orders of magnitude. In all cases, we see that both the theory and the data exhibit a global minimum at $\theta = h = 0$, which is a key prediction of the universality class ($\alpha = 0$). However, for $I_1 = 10$ (Fig. 10A) and $I_1 = 1$ (Fig. 10B) the minimum of the theory is higher than that of the data,

while for $I_1 = 0.01$ (Fig. 10D) the minimum of the theory is lower than that of the data. Only for $I_1 = 0.1$ (Fig. 10C; also Fig. 2D inset of main text) are the minima the same depth. We conclude that $I_1 = 0.1$ is the correct value, which corresponds to a value of $\bar{n}_c = 7,300$ molecules averaged across all experiments, and a value of $\bar{n}^* = 35,000$ molecules in the high mode averaged across all cases with no inhibitor.

The value of 35,000 ppERK molecules is consistent with previous measurements on these cells described in

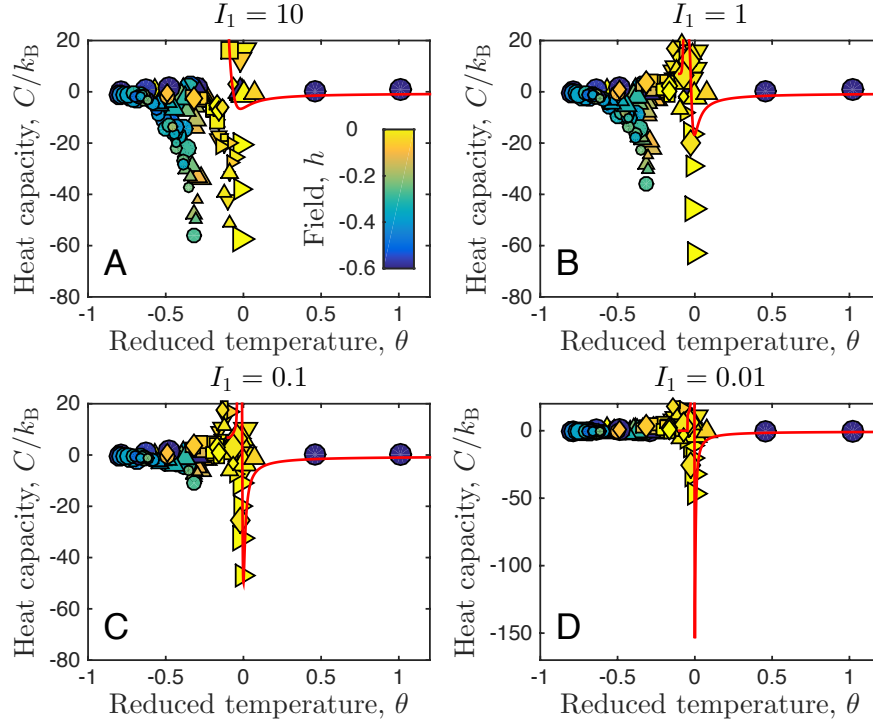


FIG. 10: Heat capacity allows determination of I_1 and therefore absolute molecule number. Titles of panels indicate values of I_1 . Only in C are depths of global minima in theory and data the same. See Table II for drugs (shape) and doses (size). Theory is for Hill model with $h = 0$ and $H = 4$.

Refs. [43] and [44] of the main text. In these references it was estimated that there are approximately 100,000 and 150,000–250,000 ERK molecules per cell, respectively, and since only about 20–30% of these molecules are doubly phosphorylated during T cell receptor activation, we arrive at the estimate of roughly 30,000–50,000 ppERK molecules per cell. Thus, the heat capacity allows one to extract I_1 unambiguously and thus allows estimation of absolute molecule number from fluorescence data.

Experimental methods

Part of the experimental data, along with a detailed description of the experimental methods, have been published previously in Ref. [4] of the main text. New data, for the quench dynamics, appears in Fig. 3 of the main text and Fig. 11 but was acquired at the same time and the same way as the published data. For the sake of completeness, in this section we briefly summarize the experimental system and methods.

The data investigate the inhibition of a complex signaling cascade, the antigen-driven MAP kinase activation in primary CD8+ mouse T cells. A natural way to stimulate T cells is to load a peptide, that is, a fragment of an antigenic protein (which the T cells are programmed to recognize), onto antigen-presenting cells. We achieve

this by incubating RMA-S cells with antigen at 37 °C. At the same time, we harvest the spleen and lymph nodes of a $RAG2^{-/-}$ OT1 mouse which has T cells specific only to the ovalbumin peptide with the amino acid sequence SIINFEKL. When we mix the OT1 T cells with the antigen-loaded RMA-S cells, we expose the OT1 T cells to their activating peptide. In response, the T cells activate their receptors through a SRC Family kinase (Lck). This triggers an enzymatic cascade, which in turn activates Ras-Raf-MEK-ERK leading to double phosphorylation of ERK, rendering it capable of communicating with the nucleus. By waiting for 10 minutes, the signaling reaches steady state and the distribution of the abundance of doubly phosphorylated ERK (ppERK), a key factor in cell regulation, is the readout in Figs. 2 and 3 of the main text. For the time-series in Fig 11 instead of waiting for the signaling to reach steady state, a relaxation time-series was sampled by applying a chemical fixative to stop chemical reactions and preserve all biomolecular states. Specifically, we administered ice cold formaldehyde in PBS to each experimental well of a 96 well-v-bottom plate such that the final working dilution is 2%, and then transferred the cell-fixative solution to a new 96 well-v-bottom plate on ice. Cells were kept on ice for 10 minutes and then precipitated by centrifugation, resuspended in ice-cold 90% methanol, and placed in a -20 °C freezer until measurements were taken.

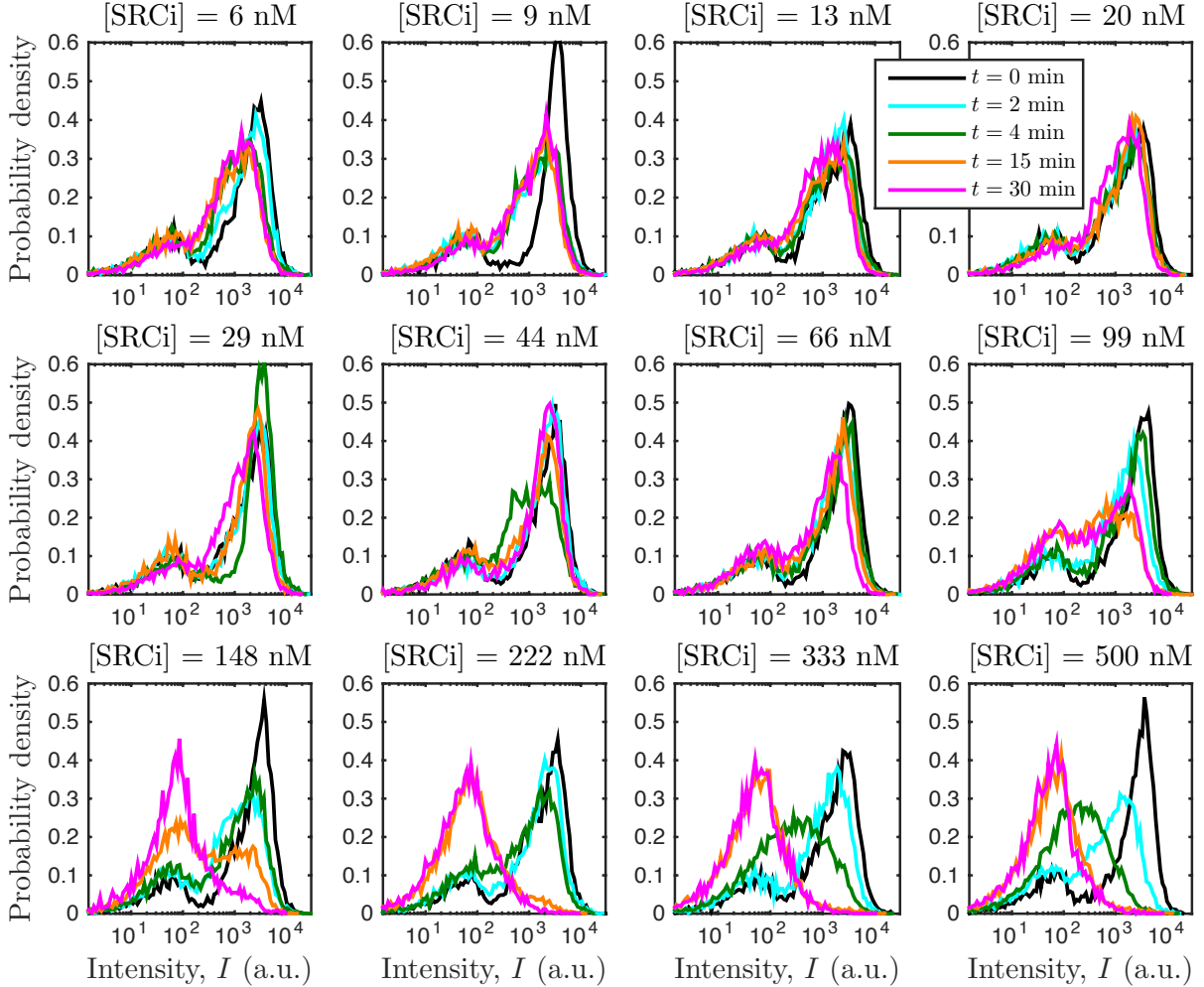


FIG. 11: Dynamics of ppERK fluorescence distribution when various doses of SRC inhibitor Dasatinib are added at time $t = 0$. Titles of panels indicate doses, which increase logarithmically from left to right. We see that when the dose is small, the distribution hardly changes (top); whereas when the dose is large, the distribution changes significantly over a finite response time (bottom).

To measure the abundance of ppERK, we use fluorescence cytometry. Specifically, we introduce ppERK-targeted antibodies that are pre-conjugated with a fluorescent dye. Because antibodies are very effective at selectively attaching to their target molecule with negligible false-positives, the fluorescence intensity of the dye is proportional to the abundance of ppERK. To measure the intensity, approximately 30,000 cells per sample are passed one-by-one through a microfluidic device where they encounter a series of excitation lasers. Each cell yields one intensity value, and the histogram provides an estimate of the distribution of ppERK abundance across the population. We assume that the distribution across the population is a fair representation of the steady-state distribution of ppERK abundance of a single cell. This is reasonable (and is the accepted practice) since while the cells are alive and the experiment is taking place, they are

in a dilute suspension (approximately 30,000 cells in 100 μL), not close enough together to influence each other.

Cells are treated with various doses of inhibitory drugs. The drugs and dose ranges used in the experiments are given in Table II. In Figs. 3(c) of the main text, 8, and 10, the size of the data point is proportional to the log of the dose, and the shape of the data point indicates the drug, as listed in Table II.

Ref. [4] describes a biologically-driven analysis of the data by fitting to a Gaussian mixture model, together with more experiments which correlate the inhibition to a functional read-out days after the stimulus. Ref. [4] also proposes a biologically-motivated coarse-grained model that relies on detailed knowledge of the MAP-kinase cascade. Here we employ an orthogonal approach: we focus on understanding the universal features, making as few assumptions as possible, and requiring no prior knowl-

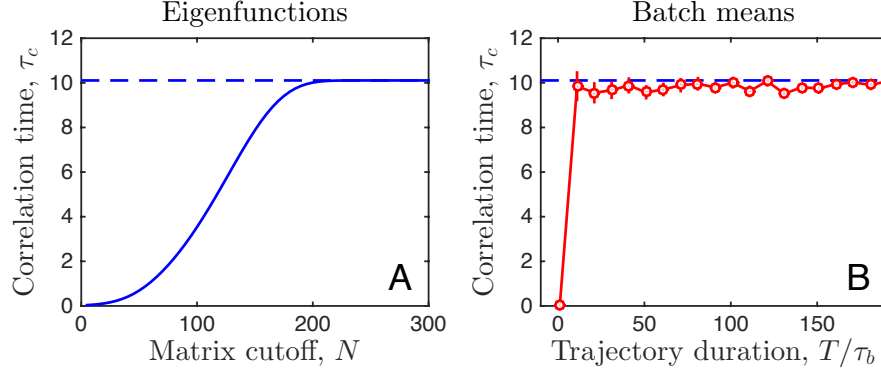


FIG. 12: Comparison of two methods to calculate correlation time: (A) numerically using eigenfunction expansion, or (B) by simulation using method of batch means. For sufficiently cutoff N or trajectory duration T , respectively, both methods converge to same value (dashed line). Data are for Schlögl model with $\theta = h = 0$ and $n_c = 100$, and time is in units of $1/k_1^-$. In B, $\tau_b = 1000$, and error bars are standard error from 50 trajectories.

edge of the biology.

Correlation time

The correlation time is defined

$$\tau_c = \frac{1}{\kappa(0)} \int_0^\infty dt \kappa(t), \quad (34)$$

where in steady state,

$$\kappa(\Delta t) = \langle n(\Delta t)n(t + \Delta t) \rangle - \bar{n}^2 \quad (35)$$

is the correlation function, and $\kappa(0) = \sigma^2$ is the variance. While it is possible to compute Eq. 35 from simulations and integrate it numerically according to Eq. 34, we find that this method is not efficient for a given accuracy. Instead, we calculate τ_c using one of two alternative methods, the first more efficient for small system sizes, and the second more efficient for large system sizes.

The first method is to calculate τ_c numerically from the master equation (Eq. 2 of the main text) by eigenfunction expansion. We write Eq. 2 as

$$\dot{\vec{p}} = \mathbf{L}\vec{p}. \quad (36)$$

where \mathbf{L} is a tridiagonal matrix containing the elements of b_n and d_n . The eigenvectors of \mathbf{L} satisfy

$$\mathbf{L}\vec{v}_j = \lambda_j\vec{v}_j, \quad (37)$$

$$\vec{u}_j\mathbf{L} = \lambda_j\vec{u}_j, \quad (38)$$

where the eigenvalues obey $\lambda_j \leq 0$ with only λ_0 vanishing for the steady state, and $\vec{v}_j^T \neq \vec{u}_j$ because \mathbf{L} is not Hermitian (Ref. [39] of the main text). Because Eq. 36 is linear in \vec{p} , the solution is

$$p_n(t) = \sum_{j n'} u_{j n'} p_{n'}(0) e^{\lambda_j t} v_{n j} \quad (39)$$

for initial condition $p_n(0)$. Calling $n(0) \equiv m$ and $n(t) \equiv n$, we write Eq. 35 as

$$\kappa(t) = -\bar{n}^2 + \sum_{mn} p_{mn} m n = -\bar{n}^2 + \sum_{mn} p_{n|m} p_m m n, \quad (40)$$

where $p_m = v_{m0}$ is the steady-state distribution, and $p_{n|m}$ is the dynamic solution at time t assuming the system starts with m molecules. That is, $p_{n|m}$ is given by Eq. 39 with initial condition $p_n(0) = \delta_{nm}$. Eq. 40 becomes

$$\kappa(t) = -\bar{n}^2 + \sum_{mn} m n v_{m0} \sum_j u_{j m} e^{\lambda_j t} v_{n j} \quad (41)$$

$$= \sum_{mn} m n v_{m0} \sum_{j=1}^{\infty} u_{j m} e^{\lambda_j t} v_{n j}, \quad (42)$$

where the second step uses orthonormality, $\sum_j v_{n j} u_{j n'} = \delta_{n n'}$, and probability conservation, $u_{0n} = 1$, to recognize that the $j = 0$ term evaluates to \bar{n}^2 . Inserting Eq. 42 into Eq. 34 and performing the integral (recalling that $\lambda_j < 0$ for $j > 0$), we obtain

$$\tau_c = \frac{1}{\sigma^2} \sum_{mn} m n v_{m0} \sum_{j=1}^{\infty} u_{j m} \left(\frac{1}{-\lambda_j} \right) v_{n j}. \quad (43)$$

In matrix notation,

$$\tau_c = \sigma^{-2} \vec{n} \mathbf{V} \mathbf{F} \mathbf{U} \vec{w}, \quad (44)$$

where \vec{n} is a row vector, $\vec{w} = m v_{m0}$ is a column vector, and neither the eigenvector matrices \mathbf{V} and \mathbf{U} nor the diagonal matrix $F_{j j'} = -\delta_{j j'} / \lambda_j$ contain the $j = 0$ term. Numerically, we compute τ_c via Eq. 44 using a cutoff $N > n_c$ for the vectors and matrices.

The second method is to calculate τ_c from a Gillespie simulation of the master equation using batch means. The idea is to divide a simulation trajectory of length

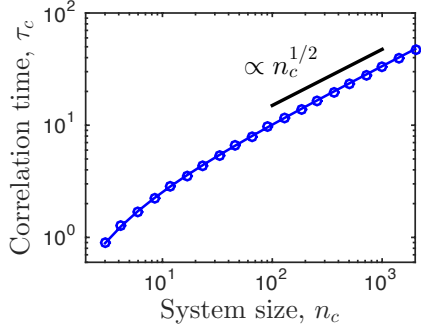


FIG. 13: Correlation time increases with system size like $\tau_c \sim n_c^{1/2}$ for large n_c . We use this relation to correct for finite-size effects during dynamic driving, as described in the text. Here τ_c is computed at $\theta = h = 0$ for the Schlögl model via Eq. 44 with matrix cutoff $N = \max(100, 3n_c)$, and time is in units of $1/k_1^-$.

T into batches of length τ_b . In the limit $T \gg \tau_b \gg \tau_c$, the correlation time can be estimated by (Ref. [48] of the main text)

$$\tau_c = \frac{\tau_b \sigma_b^2}{2\sigma^2}, \quad (45)$$

where σ_b^2 is the variance of the means of the batches.

In Fig. 12 we verify that the two methods converge to the same limit for sufficiently large N or T , respectively. We find that the first method is more efficient until $n_c \sim$

1000, when numerically computing the eigenvectors for large $N > n_c$ becomes intractable. Therefore, in Fig. 3D of the main text, we use the first method for smaller n_c (top left) and the second method for larger n_c (bottom).

Finite-size correction

Fig. 13 shows that at criticality the correlation time τ_c increases with the system size n_c , and that for large n_c we have $\tau_c \sim n_c^{1/2}$. Combining this relation with Eq. 8 of the main text, which reads

$$\tau_c|_{h=0} \sim |\theta|^{-\nu z}, \quad \tau_c|_{\theta=0} \sim |h|^{-\nu z/\beta\delta}, \quad (46)$$

and also with the dependence of θ or h on the driving time τ_d derived in the main text from the Kibble-Zurek mechanism, which reads

$$\theta \sim \tau_d^{-1/(\nu z+1)}, \quad h \sim \tau_d^{-\beta\delta/(\nu z+\beta\delta)}, \quad (47)$$

we obtain

$$n_c \sim \tau_d^{2\nu z/(\nu z+1)}, \quad n_c \sim \tau_d^{2\nu z/(\nu z+\beta\delta)}, \quad (48)$$

for driving of θ or h , respectively. We use Eq. 48 to correct for finite-size effects in Fig. 4 of the main text. Specifically, we choose n_c arbitrarily for a particular driving time τ_d , and when we choose a new τ_d , we scale n_c appropriately according to Eq. 48.